

Real-time Ionospheric Imaging of S_4 Scintillation from Limited Data with Parallel Kalman Filters and Smoothness

Alexandra Koulouri *

May 13, 2021

Abstract

In this paper, we propose a Bayesian framework to create two dimensional ionospheric images of high spatio-temporal resolution to monitor ionospheric irregularities as measured by the S_4 index. Here, we recast the standard Bayesian recursive filtering for a linear Gaussian state-space model, also referred to as the Kalman filter, first by augmenting the (pierce point) observation model with connectivity information stemming from the insight and assumptions/standard modeling about the spatial distribution of the scintillation activity on the ionospheric shell at 350 km altitude. Thus, we achieve to handle the limited spatio-temporal observations. Then, by introducing a set of Kalman filters running in parallel, we mitigate the uncertainty related to a tuning parameter of the proposed augmented model. The output images are a weighted average of the state estimates of the individual filters. We demonstrate our approach by rendering two dimensional real-time ionospheric images of S_4 amplitude scintillation at 350 km over South America with temporal resolution of one minute. Furthermore, we employ extra S_4 data that was not used in producing these ionospheric images, to check and verify the ability of our images to predict this extra data in particular ionospheric pierce points. Our results show that in areas with a network of ground receivers with a relatively good coverage (e.g. within a couple of kilometers distance) the produced images can provide reliable real-time results. Our proposed algorithmic framework can be readily used to visualize real-time ionospheric images taking as inputs the available scintillation data provided from freely available web-servers.

Keywords: Real-time ionospheric imaging, scintillation, S_4 index, GNSS system, Bayesian filtering, discrete Kalman, smoothness effect, ensemble of filters, tuning parameter

1 Introduction

The discrete time Kalman filter [32, 33] is a widely applied recursive Bayesian approach for multivariate normal distributions that allows to combine instantaneous measurements, spatial and temporal prior information to obtain estimates for a dynamically evolving system. Kalman filter, even though it was developed originally for tracking targets such as aircrafts [3], today has found applications in many research areas in engineering and signal processing [7] such as speech recognition[23], tomography [51, 17], hydrology [14] and econometrics [54] to name but a few.

*A. Koulouri was with the Faculty of Information Technology and Communication Sciences, Tampere University, P.O. Box 692, 33101 Tampere, FI, e-mail: alexandra.koulouri@tuni.fi.

The Earth’s ionospheric weather, affected by the solar activity, is a purely dynamic system whose turbulence has a significant impact on navigation, positioning and satellite communication systems that are an integral part of many human activities [44, 8]. Either Empirical [10] or physical-based models (e.g. [5]), combined with data assimilation techniques [19], have been developed to track and visualize the global ionospheric climate and weather. In particular, Kalman filtering has been proposed for example in [26, 15, 48, 19, 25] to calibrate coupled ionospheric-thermospheric physical models in order to monitor and forecast the ionospheric and plasma-spheric electron density distributions and in tomographic recovery of ionospheric total electron content (TEC).

Even though, electron density or total electron content (TEC) tomographic images can provide useful information about the ionospheric conditions, numerous ionospheric phenomena remain untracked due to the complexity and variability of the ionospheric environment [47]. For example, at lower latitudes, satellite communications using frequencies up to a few GHz can experience significant signal amplitude and phase fluctuations due to small-scale time-varying ionospheric plasma density irregularities, a phenomenon known as scintillation [16, 1, 6]. The amplitude scintillation (which is manifested as random rapid fluctuations in the signal strength) can cause periods of reduced signal power at the receiver’s antenna that can result in a power drop below the receiver-tracking threshold (loss of lock incidents) [29]. The continuous monitoring of scintillation activity especially in the equatorial area [41, 30, 31] is substantial to mitigate potential risks primarily for safety critical activities that rely on satellite communications. At the moment, this is supported by a distributed network of scintillation monitors (receivers) over South America for instance. Unfortunately, the existing network can provide scattered and sparse information about the activity over the continent. Moreover, climatology models or other numerical approaches, e.g. [46, 35, 28, 2, 34], struggle to produce real time pictures that reflect the small-scale ionospheric plasma density fluctuations due to their design or inherent limitations. For example, models may break down in the presence of strong scintillation activity [43] whereas numerical approaches often rely on collecting data over long periods of time and then illustrate an average or gross scintillation activity (e.g. averaged S_4 values) that cannot capture the scintillation spikes, spatial extent and dynamic evolution of the phenomenon. Here, we aim to address these limitations and create instantaneous ionospheric images that reflect the dynamically changing scintillation activity with the help of an enriched Kalman filter framework. To the best of our knowledge, this is the first time that S_4 amplitude/intensity ionospheric scintillation images of high spatio-temporal resolution are produced.

1.1 Our contributions

In this work, we formulate a state-space problem [39, 22] that describes macroscopically the evolution of the ionospheric scintillation activity (as measured by the S_4 index). Particularly, at each time step a standard transition model is used to express the system’s dynamics which is then corrected using a developed observation model which employs the available scintillation measurements. Our main contributions are as follows.

- We develop an observation model for the filter with the help of the finite element method [27]. Here, the measured values at pierced points are connected with a set of distributed scintillation values at fixed locations (called nodes) through linear basis functions. Hence, we produce the images on a mesh described by nodes and elements (instead of a uniform grid). The elements’ size and shape depend on the traces of the available observations on the ionospheric shell at 350 km altitude where the ionospheric images are rendered [18]. The use of linear basis functions compared to piece-wise constant functions (i.e. fixed values) as in a regular grid allows smooth transitions between neighboring nodes on the image and the capture of smaller scintillation fluctuations.
- We augment the observation model by employing a connectivity (smoothness) prior [20] (i.e. a set of extra equations) which is regularized by a tuning parameter that allow us to handle the limited available data at each time instant.
- Since, a Kalman filter requires prior knowledge about the model parameters for optimal performance [42, 21], we handle the tuning parameter choice by employing a bank of Kalman filters (here called ensemble) which run in parallel [37, 11, 36, 12]. In particular, each member of the ensemble is modeled

with a different realization for the tuning parameter (for the connectivity prior) selected from a fixed set. The output (a.k.a. the S_4 image) at each step is a weighted average of the individual filter state estimates at that time step. Our proposed scheme is based on the application of a generalized technique called assumed density filtering [38]. The weights are scalar quantities which are estimated (on-line) based on the performance of the individual filters determined using control S_4 measurements at each step. Hence, the filters with the highest weights represent the ones with the “optimal” parameter values. Compared to [45] where a weight is computed according to the performance over the entire sequence of available control measurements, here, we use only the fraction of the control data that corresponds at that particular time instant. With this scheme, we allow the weights to adjust quickly based on the most recent measurements. Moreover, we avoid underflowing problems (i.e. cases where weights tend to zero due to recursive multiplication of exponents)[45].

- We develop an algorithm that uses the proposed enriched Kalman filter framework and we produce real time images of S_4 value over South America.

We remark that the standard Kalman filter has been previously applied to reduce or mitigate scintillation effects in Global Navigation Satellite Systems (GNSS) signal tracking or precise point positioning see e.g. [9, 53, 52] and references therein. However, the developed approach, as well as the problems in question here are totally different. In particular, our work’s novelties, which are summarized to the development of an augmented state-space model that describes the spatio-temporal evolution of the scintillation activity and then the design of an ensemble of Kalman filters (in order to optimise the level of smoothness of the images), allow us to create dynamically evolving ionospheric images e.g. images of S_4 values over South America as we show in the results sections 4 and 5. These can readily be used to observe in real-time the ionospheric changes due to scintillation, can be further employed as a prior information in the estimation of dilution of precision metrics (e.g. in conjunction with the approach presented in [34]), or enrich climatology databases. We note that the developed algorithmic framework and the accompanied software can be readily used to create on-line ionospheric images taking as inputs available scintillation data provided for example from a server such as CIGALA/CALIBRA network- UNESP web server, (ISMR Query Tool [50]). In this work, we demonstrate the proposed approach by showing a sequence of S_4 images and providing a video (link). Finally, we validate the accuracy of the produced images by comparing our predictions with held-out measurements that were not included in the image estimation. We note that our approach can be readily applied in imaging other ionospheric scintillation values such as phase scintillation for instance.

2 Theory

2.1 Observation model for the ionospheric scintillation

Let us start with the model that connects the monitored scintillation data with the ionospheric scintillation activity

$$y_t = A_t s_t + \varepsilon_t, \tag{1}$$

where $y_t \in \mathbb{R}^{M_t}$ are the measured data, $s_t \in \mathbb{R}^N$ is the vector that encloses the ionospheric scintillation distribution to be estimated, $A_t \in \mathbb{R}^{M_t \times N}$ is the design matrix and $\varepsilon_t \in \mathbb{R}^{M_t}$ is the additive noise which here is modelled as Gaussian with zero mean and covariance Γ_{ε_t} i.e. $\varepsilon_t \sim \mathcal{N}(0, \Gamma_{\varepsilon_t})$. In this problem, the size M_t of the instantaneous y_t is far less than the unknown discrete distribution of s_t that is required to produce an instantaneous ionospheric image (i.e. $M_t \ll N$), therefore prior information is needed for the inversion. In the following section, we employ the discrete Kalman filter to combine instantaneous measurements with priors to estimate high resolution ionospheric scintillation images at t time steps.

2.2 Kalman Filtering

Ionospheric scintillation is a dynamic phenomenon and the quantities of primary interest are time dependant, thus we will focus on the derivation of a Bayesian scheme for the estimation of the ionospheric scintillation coefficients and the production of the corresponding images using model (1) in a non-stationary statistical framework under Gaussian assumptions. This dynamic phenomenon is expressed as a state estimation problem [20] predicted at each time step t using simple temporal evolution assumptions and then corrected with the help of scintillation observations and prior information.

2.2.1 Evolution model

Since a well-established macroscopic physics-based model, which can explicitly be described mathematically and that explains/visualizes the evolution of the scintillation phenomenon, does not exist, as a first approach to formulating the time evolution can be considered a standard state transition model which is the random walk model. By using this model, the ionospheric scintillation is assumed to remain (almost) unchanged between subsequent steps.

Hence, for the transition between states, we can enforce

$$s_t = s_{t-1} + n_t, \quad (2)$$

where the state noise n_t can be considered as a variable with a known Gaussian distribution with zero mean and covariance matrix Γ_{n_t} i.e. $n_t \sim \mathcal{N}(0, \Gamma_{n_t})$. Based on (2), we can infer that the transition probability density is

$$\pi(s_t | s_{t-1}) \propto \exp\left(-\frac{1}{2}(s_t - s_{t-1})^T \Gamma_{n_t}^{-1} (s_t - s_{t-1})\right). \quad (3)$$

2.2.2 Augmented observation model

The main bottleneck for the application of the Kalman filter is the limited number of observations in (1) (i.e. $M_t \ll N$ at every single instant t). This reduces any possibilities for estimating a time-evolving spatially distributed scintillation index s_t (i.e. we can estimate images in very limited regions which cannot be updated continuously since the available measurements cover different ionospheric areas over time). A significant improvement in the image reconstructions can be achieved by incorporating a more informative observation model into the Kalman filtering. Therefore, we propose to include spatial prior information about the scintillation index and subsequently include it into the observation model.

Here, we build up a new augmented observation model. In particular, let us assume that the scintillation values s_t can be related using a connectivity matrix $L \in \mathbb{R}^{N \times N}$ [20], then we can obtain an extra set of equations

$$Ls_t + e = 0, \quad (4)$$

where $e \in \mathbb{R}^N$ is a small perturbation term that follows a Gaussian distribution given by $e \sim \mathcal{N}(0, \lambda^{-1} I_N)$ (I_N is the identity matrix of size N) and λ a tuning parameter. Our rationale here is that often scintillation appears in the ionosphere as “clouds” and thus neighboring ionospheric regions can share almost similar scintillation activity [43].

From (4) and (1), the augmented observation model is

$$y_t^{aug} = \begin{bmatrix} y_t \\ 0 \end{bmatrix} = \begin{bmatrix} A_t \\ L \end{bmatrix} s_t + \begin{bmatrix} \varepsilon_t \\ e \end{bmatrix}. \quad (5)$$

The state-space model is described by (2) and (5) where the noise components n_t , ε_t and e are mutually uncorrelated. For this observation model, the likelihood $\pi(y_t^{aug}|s_t)$ is

$$\pi(y_t^{aug}|s_t) \propto \exp\left(-\frac{1}{2}(y_t - A_t s_t)^T \Gamma_{\varepsilon_t}^{-1} (y_t - A_t s_t) - \frac{\lambda}{2} s_t^T L^T L s_t\right). \quad (6)$$

2.2.3 Estimates using the proposed state-space model

In the Bayesian framework, we estimate the marginal posterior distribution of the state s_t at time t conditioned on the history of the observations up to the time step t [20]. If we denote all the observations up to time t as

$$D_t = \{y_1^{aug}, y_2^{aug}, \dots, y_t^{aug}\},$$

then the posterior $\pi(s_t|D_t)$ based on Bayes' rule is

$$\pi(s_t|D_t) \propto \pi(y_t^{aug}|s_t)\pi(s_t|D_{t-1}), \quad (7)$$

where $\pi(y_t^{aug}|s_t)$ is the likelihood (6) and $\pi(s_t|D_{t-1})$ is the predictive distribution since it predicts s_t at time step t given the measurements up to time $t-1$. Based on the Kalman modelling, the posterior distribution $\pi(s_t|D_t)$ is Gaussian (denoted for short by $\mathcal{N}(\hat{s}_t, \Gamma_{s_t|D_t})$) with mean \hat{s}_t and posterior covariance matrix $\Gamma_{s_t|D_t}$.

The predictive distribution $\pi(s_t|D_{t-1})$ (see further details in Appendix 6.1) is

$$\pi(s_t|D_{t-1}) \propto \exp\left(-\frac{1}{2}(s_t - s_t^*)^T \Gamma_{s_t|D_{t-1}}^{-1} (s_t - s_t^*)\right), \quad (8)$$

where the predicted vector is

$$s_t^* = \hat{s}_{t-1} \quad (9)$$

and the predicted covariance is

$$\Gamma_{s_t|D_{t-1}} = \Gamma_{n_t} + \Gamma_{s_{t-1}|D_{t-1}}, \quad (10)$$

with $\Gamma_{s_{t-1}|D_{t-1}}$ being the posterior covariance at time $t-1$.

By substituting (6) and (8) into (7) we have that the marginal posterior $\pi(s_t|D_t)$ has mean

$$\hat{s}_t = \Gamma_{s_t|D_t} (A_t^T \Gamma_{\varepsilon_t}^{-1} y_t + \Gamma_{s_t|D_{t-1}}^{-1} s_t^*), \quad (11)$$

which is the state estimate at t with $\Gamma_{s_t|D_t}$ being the posterior covariance

$$\Gamma_{s_t|D_t} = (A_t^T \Gamma_{\varepsilon_t}^{-1} A_t + \lambda L^T L + \Gamma_{s_t|D_{t-1}}^{-1})^{-1}. \quad (12)$$

3 Methodology

3.1 Single shell ionospheric model and observations

In this paragraph, we describe how a set of ground-based measurements of scintillation activity can be used in order to create images that reflect this activity on the ionosphere (tomography). Particularly, at time t we have a set of ground measurements denoted by $z_t \in \mathbb{R}^{M_t}$ where M_t is the number of available links between ground scintillation receivers and satellites at time t . To construct an ionospheric image, the ground data has to be related to the ionospheric regions. This is done by projecting the ground measurements to the ionosphere. If a projector rule is given by $P : \mathbb{R}^{M_t} \rightarrow \mathbb{R}^{M_t}$, then $y(x_{\text{ion}}(t)) = P(z_t)$, where $y(x_{\text{ion}}(t)) \in \mathbb{R}^{M_t}$ are the projected scintillation measurements at the ionospheric locations $x_{\text{ion}}(t)$ which for short are written as y_t in the following text (see Figure 1). By exploiting the

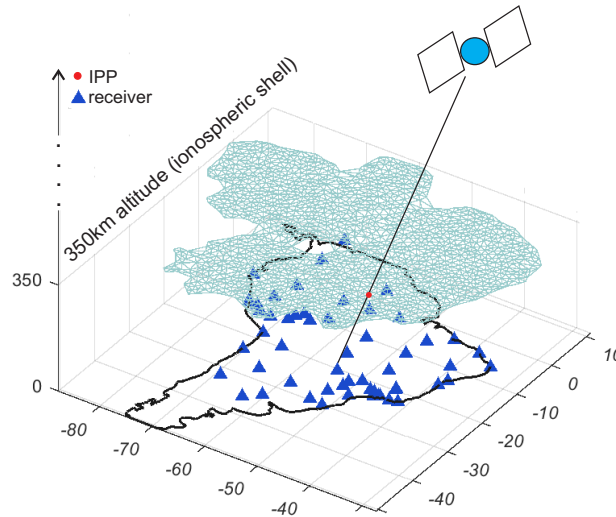


Figure 1: Direct projection of the measured data (at a ground receiver) to the ionospheric shell (red dot).

single shell model similarly as in [34] and references therein, the ground data at time t can be projected on the ionospheric layer at the corresponding ionospheric pierce points (IPPs) at 350 km (considering no angular dependency). Hence, the obtained observation vector $y_t \in \mathbb{R}^{M_t}$ includes a set of projected scintillation measurements on the ionospheric shell. Since all the ground monitors do not simultaneously produce data, we note that size M_t varies at each time step.

3.2 Linear observation model

By exploiting the finite element method (FEM), the ionospheric region, denoted by Ω , is discretized and is expressed as $\Omega \equiv (\mathcal{N}, \mathcal{T})$, where $\mathcal{N} = \{\mathbf{x}_i\}_{i=1:N}$ is the set of nodes and \mathcal{T} is the set of elements. Then, the projected scintillation measurements $y_t[j]$ can be expressed as a linear combination of basis functions ϕ_i with scintillation coefficients denoted by $s_t[j]$ at each node. Thus,

$$y_t[j] = \sum_{i=1}^N \phi_i(\mathbf{x}_j(t)) s_t[j] + \varepsilon_t[j], \quad (13)$$

for $j = 1, \dots, M_t$, where $\mathbf{x}_j(t)$ is the ionospheric location of the projected $y_t[j]$ and $\varepsilon_t[j]$ is the uncertainty introduced due to numerical approximation and unknown ionospheric disturbances. By concatenating the linear equations (13), we obtain in matrix-form the limited observation model (1). In particular, in each time step given the projected observations $y_t[j]$ we estimate the corresponding coefficients a_t^{ji} of matrix A_t in (1) where $a_t[j, i] = \phi_i(\mathbf{x}_j(t))$. Here, we use linear basis functions ϕ_i . The support of $\phi_i(\mathbf{x})$ is limited on the neighborhood of node i (i.e. only on the elements that include node i) and $\phi_i(\mathbf{x}_i) = 1$ at node \mathbf{x}_i (see Appendix 6.2).

3.3 Laplace smoothness

The available instantaneous observations are very limited, thus the evolution model has been built in such a way that it imposes connectivity and smoothness between neighboring values which then are propagated in the next time instant. This consideration is in-line with the use of the thin shell model which imposes the projection of a 3D phenomenon into a 2D plane and therefore a 2D ionospheric image reflects the scintillation activity as a result of the superposition of medium to small-scale plasma irregularities [56].

In the current implementation, matrix L in (5), is the normalized Graph Laplace [39], given by

$$L = \mathbf{I}_N - D^{-1}H, \quad (14)$$

where \mathbf{I}_N is the identity matrix of size N ; $D \in \mathbb{R}^{N \times N}$ is a diagonal matrix with diagonal elements $D_{ii} = \sum_{j=1}^N H_{ij}$; and matrix $H \in \mathbb{R}^{N \times N}$ has non zero elements for $i \neq j$, $H_{ij} = -\frac{1}{h_{ij}}$, if nodes i and j are connected (e.g. with a vertex) otherwise $H_{ij} = 0$ and $H_{ii} = 0$. Here, h_{ij} is the longitude/latitude distance between the ionospheric nodes i and j . This choice of Laplace ensures a smooth transition between neighboring nodes (in the area where measurements exist) and a uniform value for the s_t over the area where there are not any or very low influence from the available observations (since the the null space of L is the unit vector).

3.4 Initial conditions

For the observation model (5), the noise term ε_t was modelled i.i.d. Gaussian with covariance $\Gamma_{\varepsilon_t} = \gamma_\varepsilon I_{M_t}$. This error corresponds to the uncertainties introduced due to the ionospheric projection, inherent measurement errors and unknown ionospheric disturbances. In the results section 4, the used value was $\gamma_\varepsilon = 0.0018$, this value corresponds to the variance of the errors between observations $y_t[j]$ at neighboring IPPs $\mathbf{x}_j(t)$ (less than 1km distance) given time t , i.e. it was

estimated from differences of measurements, $y_{t_k}[l] - y_{t_k}[j]$ when their corresponding IPPs satisfied $\|x_l(t_k) - x_j(t_k)\|_2 \leq 1$ km (in Cartesian coordinates). For the evolution model (2), the covariance of the perturbation N_t was modelled as $\Gamma_{n_t} = \gamma_n I_N$. Here, γ_n was set equal to the variance of the difference of consecutive observations corresponding to the same satellite-ground monitor link. Finally, following the Kalman filter initial condition $\pi(s_0|D_0) = \pi(s_0)$, we set $\Gamma_{s_1|D_0} = \Gamma_{n_t}$ and $\hat{s}_0 = 0$.

3.5 Ensemble of Kalman filters

The selection of a tuning parameter λ is not a trivial task particularly in a time varying problem. Here, we employ the multiprocess modelling concept [39, 37] and we introduce an ensemble of P state-space models ((2) and (5)), each one indexed by an indicator p with a tuning parameter λ taken from a discrete set of values λ_p for $p = 1, \dots, P$ (where P is the total number of tuning parameters). The basic idea of using an ensemble of state-space models is that a priori no constant tuning parameter λ is expected to hold for all time instances t . Therefore, by obtaining estimates at each time t using different tuning parameters and then estimating a weighted average (with weights relying on control data as we shall see next), we can overcome the λ selection problem. Figure 2 illustrates the proposed pipeline.

In particular, the moments (mean and covariance) of each member of the ensemble are obtained by running in parallel P Kalman filters, each conditional on the state of $\lambda = \lambda_p$. Then, an ionospheric scintillation image is estimated at t as a weighted average

$$\hat{s}_t^w = \sum_{p=1}^P w_t^{(p)} \hat{s}_t^{(p)}, \quad (15)$$

where $\hat{s}_t^{(p)} \in \mathbb{R}^N$ is the mean of the p^{th} member given λ_p and $w_t^{(p)} > 0$ are weights, showing our confidence on the selected λ_p . The weights can be estimated on-line using the residuals between available held-out data and predicted estimates obtained from the P Kalman filters. Furthermore, the uncertainty in the estimates (15) can be quantified with the weighted covariance matrix

$$\begin{aligned} \Gamma_t^w &= \mathbb{E}[(s_t - \hat{s}_t^w)(s_t - \hat{s}_t^w)^T] \\ &= \sum_{p=1}^P w_t^{(p)} (\Gamma_{s_t|D_t}^{(p)} + (\hat{s}_t^{(p)} - \hat{s}_t^w)(\hat{s}_t^{(p)} - \hat{s}_t^w)^T). \end{aligned} \quad (16)$$

Then, the ensemble of Kalman filters is described in Algorithm 1. Based on Algorithm 1, the weighted mean and covariance are used at the prediction step of the ensemble members. In effect here we have a hybrid model that expresses our belief state with a mixture of P Gaussians [4] which is approximated as a single Gaussian [38, 40].

Algorithm 1 Sequence of ionospheric scintillation images using parallel Kalman filters

Initialization: $\hat{s}_0^w = 0$, $s_0^{(p)} = 0 \in \mathbb{R}^N$, $\{\lambda\}_{p=1:P}$, $\Gamma_{n_t} = \gamma_n I_N$, $\Gamma_{\varepsilon_t} = \gamma_\varepsilon I_{M_t}$ and $\Gamma_0^w = 0$.

for $t = 1 \dots$ **do**

▷ for every minute

Estimate the nonzero coefficients of matrix A_t using the available data y_t ;

for $p = 1 : P$ **do**

▷ run parallel Kalman filters

Set $s_t^{(p)*} = \hat{s}_t^w$ and $\Gamma_{s_t|D_{t-1}}^{(p)} = \Gamma_{n_t} + \Gamma_t^w$

▷ prediction step

Estimate member's covariance: $\Gamma_{s_t|D_t}^{(p)} = (A_t^T \Gamma_{\varepsilon_t}^{-1} A_t + \lambda_p L^T L + \Gamma_{s_t|D_{t-1}}^{(p)-1})^{-1}$

Estimate member's mean: $\hat{s}_t^p = \Gamma_{s_t|D_t}^{(p)} (A_t^T \Gamma_{\varepsilon_t}^{-1} y_t + \Gamma_{s_t|D_{t-1}}^{(p)-1} s_t^{(p)*})$

▷ updates

end for

Estimate the weights $w_t^{(p)}$ as described in section 3.5.1 using control data $y^c(t)$.

Estimate scintillation image: $\hat{s}_t^w = \sum_{p=1}^P w_t^{(p)} \hat{s}_t^{(p)}$

Estimate covariance: $\Gamma_t^w = \sum_{p=1}^P w_t^{(p)} (\Gamma_{s_t|D_t}^{(p)} + (\hat{s}_t^{(p)} - \hat{s}_t^w)(\hat{s}_t^{(p)} - \hat{s}_t^w)^T)$

end for

3.5.1 Estimation of the weights

From Bayes' rule [12, 20], the weights in (15) can be expressed as probability densities $w_t^{(p)} = \pi(\lambda_p | y_t^c)$ where

$$\pi(\lambda_p | y_t^c) = \frac{\pi(y_t^c | \lambda_p) \pi(\lambda_p)}{\sum_{p=1}^P \pi(y_t^c | \lambda_p) \pi(\lambda_p)}. \quad (17)$$

Here, $y_t^c \in \mathbb{R}^{M_{c_t}}$ denotes a set of control data of size M_{c_t} that was not used to estimate each (member's) mean $\hat{s}_t^{(p)}$, and covariance $\Gamma_{s_t|D_t}^{(p)}$.

Without prior information about the value of the tuning parameter, we can consider that λ_p are uniformly distributed i.e. $\pi(\lambda_p) = 1/P$. Thus,

$$w_t^{(p)} = \frac{\pi(y_t^c | \lambda_p)}{\sum_{p=1}^P \pi(y_t^c | \lambda_p)}. \quad (18)$$

The conditional densities are modelled as Laplace distributions

$$\pi(y_t^c | \lambda_p) \propto \exp \left(- \sum_{m=1}^{M_t^c} \kappa_m |y_t^c[m] - \hat{y}_t^{(p)}[m]| \right), \quad (19)$$

with $\kappa_m = \left(\sqrt{\frac{1}{2P} \sum_{p=1}^P (y_t^c[m] - \hat{y}_t^{(p)}[m])^2} \right)^{-1}$ and $\hat{y}_t^{(p)}$ being the member prediction estimated from $\hat{y}_t^{(p)} = \hat{A}_t \hat{s}_t^{(p)}$, where $\hat{s}_t^{(p)}$ is the mean of the p^{th} member and where \hat{A}_t includes the basis coefficients for the IPP of measurement y_t^c . Here $[m]$ denotes the m^{th} entry of vector y_t^c and $\hat{y}_t^{(p)}$. Therefore, the weights are estimated based on the corresponding residuals (between the prediction and control data). We note that the heavier tails of the Laplace distribution (compared to e.g. a Gaussian distribution which would be the alternative standard option) can handle better extreme cases, where control data does not fully agree with the predictions.

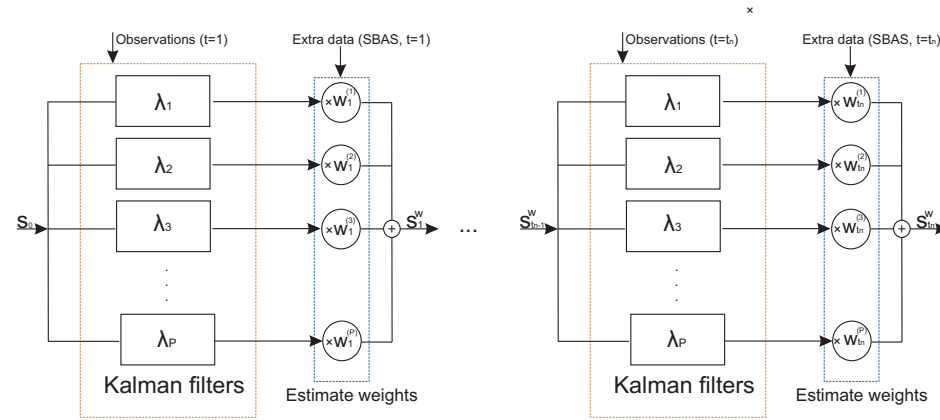


Figure 2: Pipeline of the proposed ensemble of Kalman filters.

4 Data and dynamic scintillation imaging

In this section, we describe the available data and present dynamic ionospheric scintillation images in the area of South America at geographic latitude between $\sim -40^\circ\text{N}$ and $\sim 10^\circ\text{N}$ and longitude between $\sim -90^\circ\text{E}$ and $\sim -35^\circ\text{E}$. These regions experience the most significant amplitude scintillation activity mostly after sunset until a few hours after midnight local time. We believe that creating real time ionospheric images at 350 km estimated using S_4 data in this area is rather important.

4.1 Available data

The S_4 data (that was used to produce ionospheric images) was measured from a network of 36 ISMR scintillation receivers using all the available satellite systems i.e. the Global Positioning System (GPS), Globalnaya Navigazionnaya Sputnikovaya Sistema, (GLONASS), Galileo (European navigation system) and Satellite-based Augmentation System (SBAS). In particular, the S_4 (L1) measurements (with sampling period $t = 1$ minute), the links (satellites-station names) and their IPPs at 350 km were downloaded from the CIGALA/CALIBRA network - UNESP web server [50, 13] (we note that the downloaded data was used as such without applying any post-processing step). Each instant image was produced using as y_t observations, the S_4 measurements available within that specific minute. The period that the images were produced was during the night time between 01 and 02 December 2014, a period of time which was characterized by mild to strong scintillation according to the information provided by the ISMR Query Tool ([http:// is-cigala-calibra.fct.unesp.br](http://is-cigala-calibra.fct.unesp.br)) [50].

4.1.1 Control data for the weights

Approximately 10% of the remaining S_4 data, which was available at every minute and corresponded to 19 real-time measurements from the SBAS system, were used to estimate the weights in the ensemble of Kalman filters. The SBAS data was chosen for the weighting because it was continuously available for the same set of (ground receiver-SBAS satellite) links with fixed IPP locations on the ionospheric shell. The locations of the IPPs of these 19 measurements appear in Figure 3.

4.2 Image construction over South America

Instead of a regular grid which restricts the ability for adaptations around the locations where there is constant information, we used a triangular mesh to construct the ionospheric scintillation images where we defined smaller and larger elements based on the availability of the observations in the different ionospheric locations. The number of the nodes of the mesh and their locations was based on the availability of the projected S_4 measurements over the time interval that the images were produced.

To estimate the mesh, we performed the following steps. We plotted all the available IPPs over a period of time (i.e. 6 hours) in order to identify the region where there is available data. Then, we marked all the IPPs that lied on the boundaries of the ionospheric area to define the borders of the mesh. Subsequently, we down-sampled the IPPs using a circle of radius R , i.e. we started from one boundary IPP, we discarded all the IPPs within a circle of radius $R = 1$ (in units of longitude and latitude) with center this IPP, and we kept the IPP which was the closest to the current one and outside of the circle. Then, we used this new point in a similar fashion to estimate the next point. The downsampled IPPs were used as the nodes of the created Delaunay triangular mesh (also the long deformed

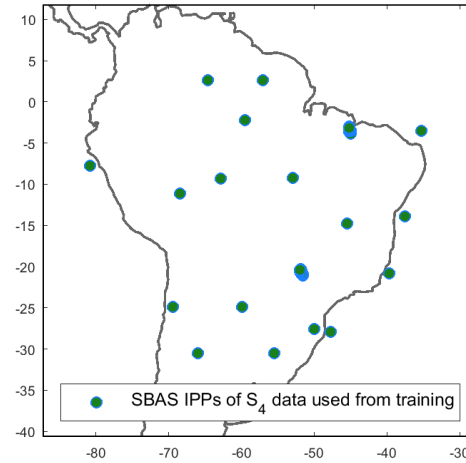


Figure 3: The IPPs of the SBAS control data.

elements created by boundary nodes were discarded). To avoid very small elements on the boundary, we applied the Taubin's mesh smoothing [49]. The nodes of the constructed mesh were the locations where the values s_t^w (15) were estimated. Figure 4 illustrates on the left the original distribution of IPPs, the border marked with orange color, the created nodes in red color and on the right we have the final mesh.

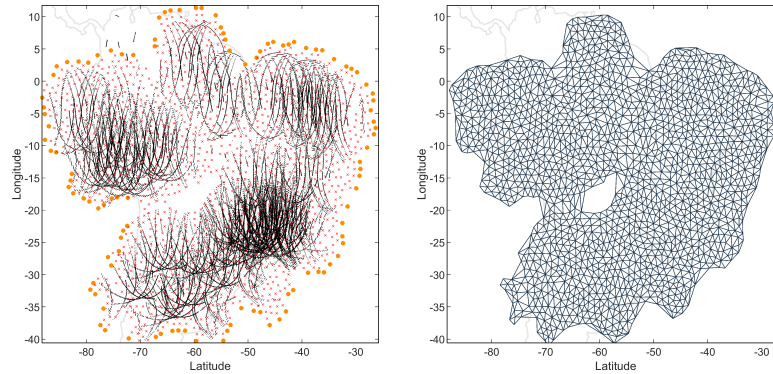


Figure 4: Left: Distribution of IPPs over 6 hours (and corresponding borders marked in orange color and nodes in red crosses). Right: Constructed mesh used in the estimation of ionospheric scintillation images.

4.3 Real-time scintillation imaging

To create the ensemble of Kalman filters, we employed 13 tuning values λ_p ranging from 10^{-3} to 500. This range was selected in order to avoid over-smoothing the covariance (12). In Figure 5, we can see instantaneous ionospheric scintillation images over South America during the night-time between December 1 and 2, 2014. Each image depicts the estimated S_4 distribution on the mesh, employing only the S_4 measurements that were available at a minute interval provided above each picture in Universal Time (UT). The blank space indicates an area where there was no coverage from the current GNSS system. As we can see the highest scintillation activity is observed over the equatorial anomaly and especially over Brazil. The activity is low early in the evening while it increases during the beginning of the night over each region of the continent (we could see that by converting the UT to local times). These observations are in line with the static risk maps presented in our previous work [34].

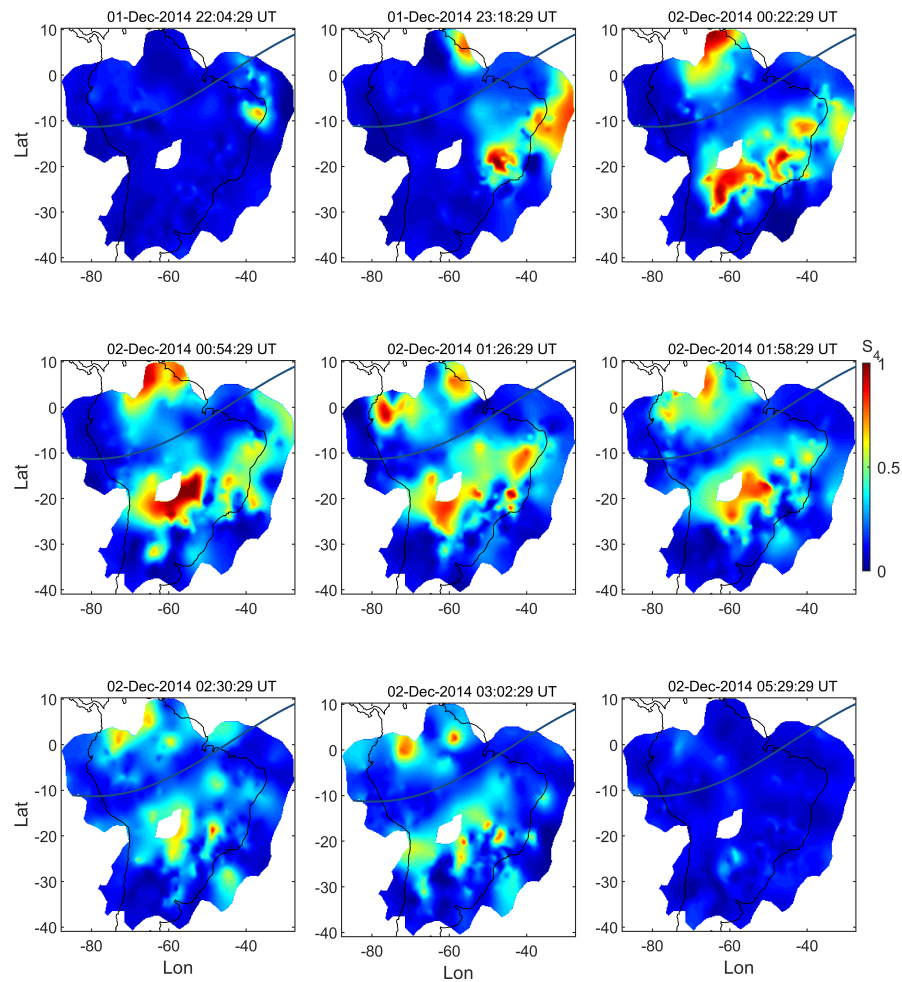


Figure 5: Sequence of S_4 ionospheric images (snapshots) during the night-time between December 1 and 2, 2014. The dark line indicates the magnetic equator.

5 Cross-validation tests and analysis

To validate the accuracy of our modelling, we compare sequences of real measurements (obtained from given satellite-receiver links) with predictions estimated using the produced images. In particular, we used the cross-validation technique i.e. we produce a sequence of ionospheric maps \hat{s}_t without including the scintillation data from a test satellite-receiver link (a.k.a. left-out link). Then, we use the ionospheric image and the given IPP for the left-out link to estimate the scintillation values for this particular link over time and then we compare our predictions \hat{y}_t , with the measurements y_t^r (validation data). The same was repeated for different satellite-monitor links as we can see in this section. The sequence of the predicted values for a link k was estimated by $\hat{y}_t[k] = \sum_{i=1}^N \phi_i(\mathbf{x}_k^r(t)) \hat{s}_t^w[i] = A_t^{k,:} \hat{s}_t^w$, where $A_t^{k,:} \in \mathbb{R}^{1 \times N}$ is a row vector that includes the basis coefficients for a given IPP $\mathbf{x}_k^r(t)$, and \hat{s}_t^w is the estimated weighted ionospheric image at time t . The numerical standard deviation was estimated as $\sigma_t[k] = \sqrt{A_t^{k,:} [\sum_{p=1}^P w_t^{(p)} (\hat{s}_t^{(p)} - \hat{s}_t^w) (\hat{s}_t^{(p)} - \hat{s}_t^w)^T] (A_t^{k,:})^T}$. For the numerical comparison, we employed two metrics: the data-model correlation metric (CM)

$$C_{\hat{y}, y^r} = \frac{1}{T} \frac{1}{\sqrt{\gamma_{\hat{y}}}, \sqrt{\gamma_{y^r}}} \sum_{t=0}^T (\hat{y}_t - \langle \hat{y} \rangle) (y_t^r - \langle y \rangle), \quad (20)$$

where $\langle \cdot \rangle$ denotes the mean values and γ are the sample variances of the estimates \hat{y} and measured S_4 values y^r and the Root-mean-square error (RMS)

$$e_{\text{rms}} = \sqrt{\frac{1}{T} \sum_{t=1}^T (\hat{y}_t - y_t^r)^2}, \quad (21)$$

which gives the difference between the model estimation and the actual system activity.

In the following, we compare our predictions (from the created images) against the measured S_4 values from two ground receivers 14 and 53 that were not used in the image estimation (the numbering of the receivers is based on the receiver database available in [50]). The locations of these receivers are shown in Figure 6. The receiver 14 was chosen because it is surrounded by other nearby ground receivers, and receiver 53 because it is located remotely i.e. there are less ground receivers nearby. As a result, the effect of the spatial density of available observations on the accuracy of the estimated images can be showcased. Figure 7 shows the IPPs of the available observations that were used to produce the predicted S_4 values.

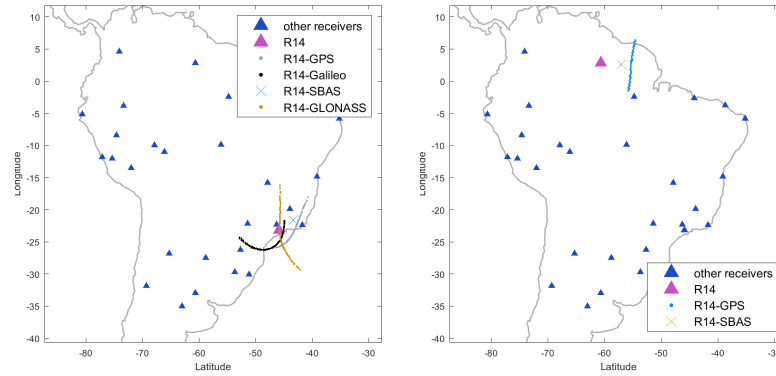


Figure 6: Left: Location of receiver 14 and the corresponding IPPs at 350km between 14 and satellites S120 (SBAS), G29 (GPS), R6 (GLONASS), E12 (Galileo). Right: Location of receiver 53 and the corresponding IPPs between 53 and S120 (SBAS) and G29 (GPS).

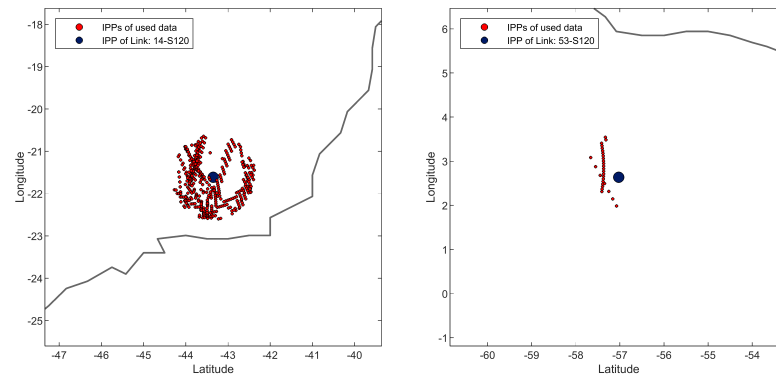


Figure 7: The small dots show the IPPs of the available observations that were used to produce the image (in a circle of radius one) around the IPPs of link R14-S120 (left image) and link R53-S120 (right image).

5.1 Receiver 14

In Figures 8 we present the results for links between receiver 14 and satellites S120 or R5 and in Figure 9, we have the links between receiver 14 and satellites G29 or E12 respectively. Here, S120 stands for satellite no 120 of the SBAS constellation, R5 for a satellite of GLONASS system, G29 for GPS system and E12 for Galileo system respectively. First, in the upper graph of Figure 8 we observe the accuracy of our images to predict the S_4 value of link 14-S120 by comparing

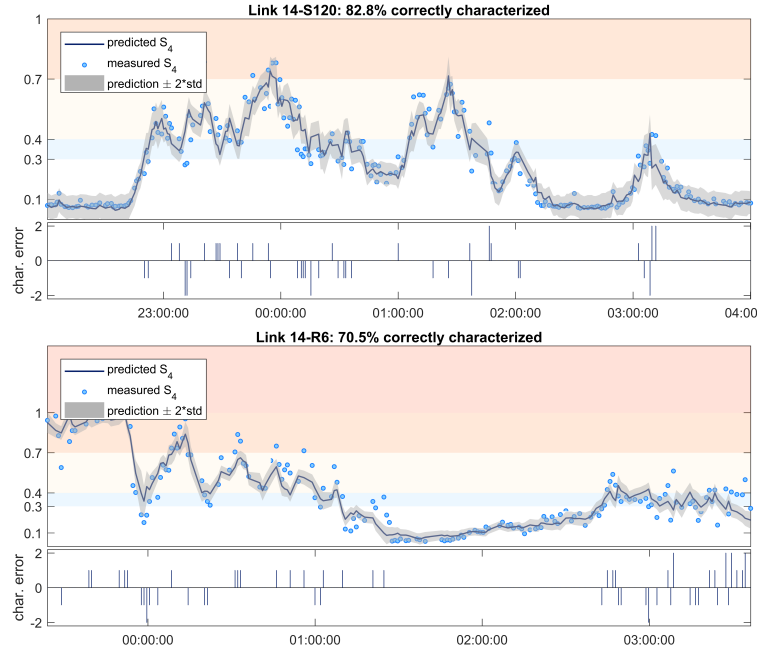


Figure 8: Comparisons between measurements and predictions for links between a ground receiver 14 and 2 satellites over the night Dec. 1-2, 2014. For each link, the top figure show the time series of the predicted S_4 values (black line) versus the measured values (blue circles). The grey area shows the two standard deviation interval around the predictions. The shaded colors depict the different scintillation characterisation levels (strong: $S_4 > 0.7$, moderate: $0.4 < S_4 \leq 0.7$, weak: $0.3 < S_4 \leq 0.4$, very weak: $S_4 \leq 0.3$). Under each time series is the discrepancy between predictions and measurements in terms of scintillation characterization levels 1, 2 etc.

the estimates (predictions) to the measured S_4 data (marked with light blue circles). Also, we plot the estimated 2 standard deviation interval around our predictions (in gray colour). This graph has been divided horizontal zones with different colours which indicate the severity of scintillation activity. In particular, the white zone indicates the level where there is very weak scintillation activity ($0 \leq S_4 < 0.3$), the light blue zone designates the level with weak scintillation

($0.3 \leq S_4 < 0.4$), the light yellow zone designates the level with moderate activity ($0.4 < S_4 \leq 0.7$), the light orange corresponds to the level with strong activity ($0.7 \leq S_4 \leq 1$) and the red zone is for values above 1 (the characterization zones are based on [52]). Moreover, under the time series graph, we have an error bar graph that depicts the errors in scintillation characterization between the measurements and predictions at each time step t . In particular, when the observed measurements (validation data) and the prediction at time t belong to the same scintillation zone then we say that the scintillation characterization (for example, strong, moderate, weak and very weak) is the same both for the prediction and the true measurement and then the characterization error is 0. On the other hand, when the characterization differs between the two data points then this error is quantified as level 1 or 2 (if a prediction gives lower scintillation activity than the measured data) and -1 or -2 (if the prediction is in a higher zone than the measured data). For instance, if a prediction at time t is located in the moderate zone and the measured data is located in the weak zone then the error is -1. Moreover, above each time series graph we have included the percentage of the predictions that were in the correct scintillation zone. to moderate scintillation activity our predictions are optimal (e.g. link 14-G29 or 14-E12) while there are some measurements ... Similar graphs we have for the links 14-G29 and 14-E12 in Figure 9. Overall, we can observe that the predictions are in accordance

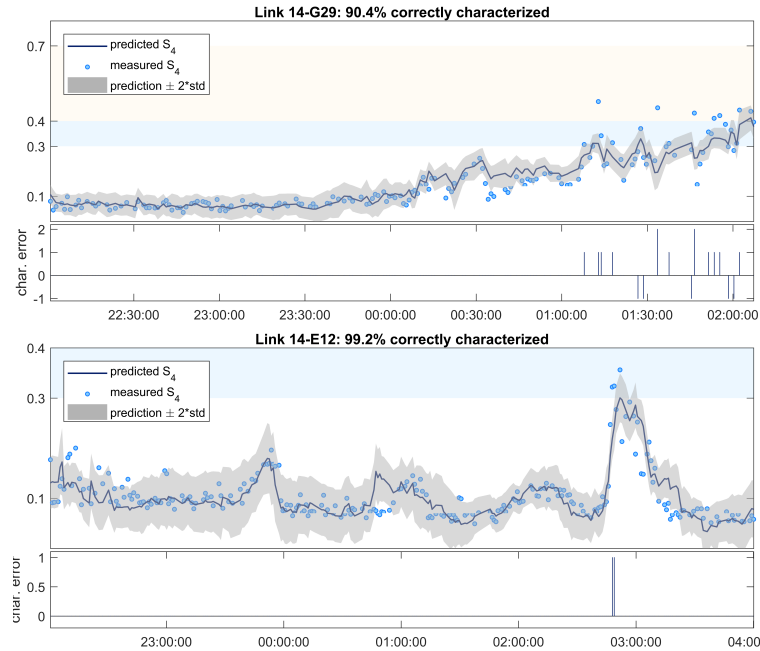


Figure 9: Similar description as in Fig. 8 for the links R14-G29 (GPS) and R14-E12 (Galileo)

with the actual measurements with small deviations and inaccuracies when abrupt changes in the scintillation activity take place (e.g. large jumps in consecutive measurements) for all the tested links related to receiver 14.

5.2 Receiver 53

Similarly as in the previous subsection, we compare predictions with measurements for two links that have far less available data and scintillation monitors around them based on Figure 6 and 7 (right images). Overall in Figure 10 we can observe that our predictions are less accurate when there is not enough available S_4

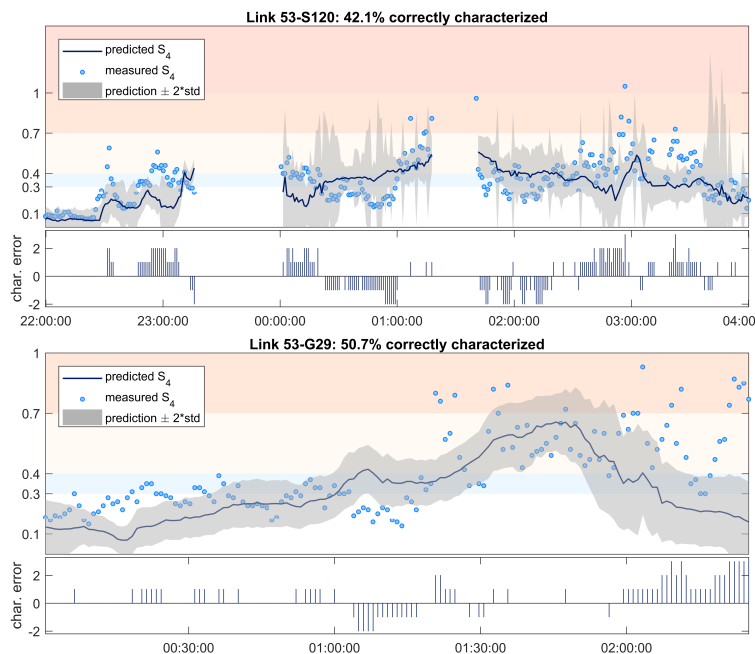


Figure 10: Top and bottom figures are similar as in Fig. 8. Time series of the predicted S_4 values (black line) versus measured values (blue circles) for ground receiver 53 and 2 satellites (S120-SBAS and G29-GPS) during the night Dec. 1-2, 2014.

data in the vicinity of these links. For weak to moderate scintillation activity our algorithm works within a good tolerance. However, we can see large standard deviations and low percentages for correct scintillation characterization as it was expected due to the limited available data and difficulty to capture abrupt changes or high scintillation activity. For the link 53-G29, we have that the prediction curve is relatively smooth following the measurements until 1.45 pm.

However, after 2.00 am it misses the scintillation activity due to the lack of available coverage in this ionospheric region. Interestingly for the link 53-S120 (SBAS) we can observe that there are periods where there are not available measurements but unfortunately we are not aware why this is happening.

5.3 Validation metrics

In table 1, we quantify the results presented in Figures 8, 9 and 10 with the help of the CM (20) and RMS (21) metrics. As it was expected the correlation is large and the RMS is low for the links related to receiver 14 while the values of these metrics are large for receiver 53. Based on our results, we can conclude that the proposed approach can produce images with good spatial and temporal resolution with high accuracy in these ionospheric areas where there is a good spatial and temporal coverage most of the time (i.e. small data gaps over time and relatively small spatial distance e.g. 1 or 2 units of degree in longitude/latitude). This can be achieved by installing extra ground receivers and ideally by creating a dense spatially uniform distributed network of scintillation monitors which unfortunately currently is not available. This would be important for creating robust real time scintillation images everywhere over the continent which could provide critical information during the time interval where strong scintillation activity takes place, especially at the anomaly.

Link	14-S120	14-R5	14-G29	14-E12	53-S120	53-G29
CM	0.95	0.94	0.92	0.81	0.39	0.44
RMS	0.062	0.097	0.043	0.03	0.18	0.21
Cor.%	82.8	70.5	90.4	99.2	42.1	50.7

Table 1: CM, RMS between the measurements and predictions and percentage of correct characterization in the predefined scintillation zones during the night time between 1-2 Dec. 2014 for the links presented in Fig. 8, 9 and 10.

5.4 Ensemble vs. single Kalman filter

Finally, we present the predictions that we would have obtained if we were running algorithm 1 with single tuning parameters. Based on Figure 11, we see that the prediction curves do not differ significantly when using single tuning parameters (instead of the ensemble) for the link 14-S120 due to the constant availability of observations. However, by comparing the percentage of correctly characterized scintillation activity for the link 53-S120, we have that the ensemble (Figure 10) performs better than the single kalman filters (Figure 11). Moreover, for the link 53-S120 in Figure 11, we can see a large variation in the predictions for single tuning parameters. This is because the Laplace smoothness (4) affects strongly the S_4 distribution at the ionospheric area around 53-S120. Large λ will impose spatial smoothness on this area while small values force a constant value on the same area.

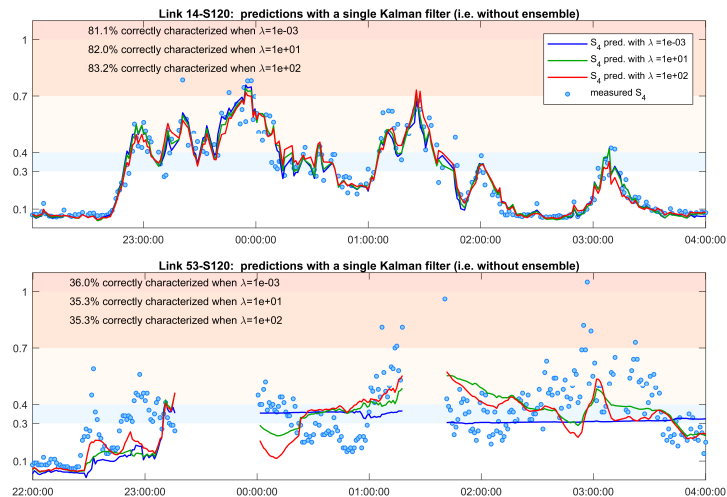


Figure 11: Predictions obtained by running a Kalman with a single tuning parameter λ .

6 Conclusions and future work

In this work, we proposed an algorithm that employed the Kalman modelling in conjunction with numerical and learning techniques to produce ionospheric S_4 images of high temporal and spatial resolution. We demonstrated our approach by producing scintillation images over South America during the night-time 1-2 December 2014 which was a period of mild to strong scintillation activity. We validated the accuracy of our images by comparing estimates (based on our images) with measurements that were not used to produce these images. Our results saw that we can predict with a very high accuracy the S_4 values (i.e. both weak and strong activity) in ionospheric areas where there is a fairly good coverage by ground receivers. We remark that our approach can be directly applied for scintillation monitoring (e.g. amplitude, phase or variance of TEC) over other areas which are suffering of communication disruptions due to scintillation e.g. over the Scandinavian peninsula and Finland. Furthermore, to increase the accuracy of our images, our approach could include other data e.g. occultation measurements [24, 55]. Regarding our proposed framework, there are several modifications which could be considered in the future. For example, we could update dynamically the set of the tuning parameters as in [12]. Moreover, the noise covariance matrices in (2) and (5) could be estimated using learning techniques [39]. Another point is the production of 3D images or to introduce another matrix L instead of (14); however all the previous ideas require extra data which could be acquired if more scintillation receivers and satellites become available in the future.

Acknowledgement

The work was supported by the Academy of Finland Postdoctoral Researcher program (No 316542). I would like to cordially thank Dr. N. D. Smith for his suggestions how to handle the unknown tuning parameter, providing comments and our fruitful discussions. Also, I would like to thank Dr. V. Rimpiläinen for reading my manuscript, proposing improvements and helping to edit the results sections.

References

- [1] J. Aarons. Global morphology of ionospheric scintillations. *Proceedings of the IEEE*, 70(4):360–378, apr 1982.
- [2] L. Alfonsi, G. Povero, L. Spogli, Cl. Cesaroni, B. Forte, C. N. Mitchell, R. Burston, Sr. V. Veetil, M. Aquino, V. Klausner, M. T. A. H. Muella, M. Pezzopane, Al. Giuntini, I. Hunstad, G. De Franceschi, E. Musico, M. Pini, V. La The, H. Tran Trung, A. Husin, Sr. Ekawati, Ch. Victoria de la Cruz-Cayapan, M. Abdullah, N. M. Daud, Le H. Minh, and N. Floury. Analysis of the regional ionosphere at low latitudes in support of the biomass ESA mission. *IEEE Transactions on Geoscience and Remote Sensing*, 56(11):6412–6424, nov 2018.
- [3] B. Alsadik. Kalman filter. In *Adjustment Models in 3D Geomatics and Computational Geophysics*, pages 299–326. Elsevier, 2019.
- [4] D. Alspach and H. Sorenson. Nonlinear bayesian estimation using gaussian sum approximations. *IEEE Trans. Automat. Contr.*, 17(4):439–448, aug 1972.
- [5] M. J. Angling and N. K. Jackson-Booth. A short note on the assimilation of collocated and concurrent GPS and ionosonde data into the electron density assimilative model. *Radio Science*, 46(6), jul 2011.
- [6] M. Aquino, T. Moore, Al. Dodson, S. Waugh, J. Souter, and F. S. Rodrigues. Implications of ionospheric scintillation for gnss users in northern europe. *J. Navig.*, 58(2):241 – 256, 2005.
- [7] Fr. Auger, M. Hilaret, J. M. Guerrero, E. Monmasson, T. Orlowska-Kowalska, and S. Katsura. Industrial applications of the kalman filter: A review. *IEEE Trans. Ind. Electron.*, 60(12):5458–5471, dec 2013.
- [8] J. L. Awange. *Environmental Monitoring using GNSS*. Springer Berlin Heidelberg, 2012.
- [9] V. Barreau, W. Vigneau, Ch. Macabiau, and L. Deambrogio. Kalman filter based robust GNSS signal tracking algorithm in presence of ionospheric scintillations. In *2012 6th ESA Worksh. on Sat. Nav. Techn. (Navitec 2012) & Eur. Worksh. on GNSS Sig. and Sig. Proc.*, dec 2012.
- [10] D. Bilitza, K. Rawer, and S. Pallaschke. Study of ionospheric models for satellite orbit determination. *Radio Science*, 23(3):223–232, may 1988.
- [11] H.A.P. Blom and Y. Bar-Shalom. The interacting multiple model algorithm for systems with markovian switching coefficients. *IEEE Trans. Automat. Contr.*, 33(8):780–783, 1988.
- [12] W.S. Chaer, R.H. Bishop, and J. Ghosh. A mixture-of-experts framework for adaptive kalman filtering. *IEEE Trans. on Systems, Man and Cybernetics, Part B (Cybernetics)*, 27(3):452–464, jun 1997.
- [13] CIGALA/CALIBRA. Monitoring stations from the network were deployed in the context of the Projects CIGALA and CALIBRA, both funded by the European Commission (EC) in the framework of the FP7-GALILEO-2009-GSA and FP7-GALILEO-2011-GSA-1a, respectively, and FAPESP Project Number 06/04008-2.
- [14] M. P. Clark, D. E. Rupp, R. A. Woods, X. Zheng, R. P. Ibbitt, A. G. Slater, J. Schmidt, and M. J. Uddstrom. Hydrological data assimilation with the ensemble kalman filter: Use of streamflow observations to update states in a distributed hydrological model. *Advances in Water Resources*, 31(10):1309–1324,

oct 2008.

- [15] S. M. Codrescu, M. V. Codrescu, and M. Fedrizzi. An ensemble kalman filter for the thermosphere-ionosphere. *Space Weather*, 16(1):57–68, jan 2018.
- [16] R.K. Crane. Ionospheric scintillation. *Proc. of the IEEE*, 65(2):180–199, 1977.
- [17] K. J. Daun, St. L. Waslander, and Br. B. Tulloch. Infrared species tomography of a transient flow field using kalman filtering. *Applied Optics*, 50(6):891, feb 2011.
- [18] Kenneth Davies. *Ionospheric Radio*. Institution of Engineering & Technology, 1990.
- [19] S. Elvidge and M. J. Angling. Using the local ensemble transform kalman filter for upper atmospheric modelling. *J. Space Weather. Space*, 9:A30, 2019.
- [20] Jari P. Kaipio Erkki Somersalo. *Statistical and Computational Inverse Problems*. Springer-Verlag GmbH, 2006.
- [21] R. Fitzgerald. Divergence of the kalman filter. *IEEE Trans. Automat. Contr.*, 16(6):736–747, dec 1971.
- [22] Sylvia Frahwirth-Schnatter. *Finite Mixture and Markov Switching Models*. Springer-Verlag GmbH, 2006.
- [23] Sharon Gannot. Speech enhancement: Application of the kalman filter in the estimate-maximize (EM) framework. In *Signals and Communication Technology*, pages 161–198. Springer-Verlag, 2005.
- [24] K.M. Groves, F.H. Ruggiero, M.J. Starks, T.L. Beach, and P. Strauss. Comparisons of space-based gps occultation ionospheric scintillation measurements with ground-based vhf measurements. In *11th International Congress of the Brazilian Geophysical Society*. European Association of Geoscientists & Engineers, 2009.
- [25] J. He, X. Yue, H. Le, Z. Ren, and W. Wan. Evaluation on the quasi-realistic ionospheric prediction using an ensemble kalman filter data assimilation algorithm. *Space Weather*, 18(3), mar 2020.
- [26] C.-T. Hsu, T. Matsuo, X. Yue, T.-W. Fang, T. Fuller-Rowell, K. Ide, and J.-Y. Liu. Assessment of the impact of FORMOSAT-7/COSMIC-2 GNSS RO observations on midlatitude and low-latitude ionosphere specification: Observing system simulation experiments using ensemble square root filter. *J. Geophys. Res. Space Phys.*, 123(3):2296–2314, mar 2018.
- [27] Th. Hughes. *Finite Element Method: Linear Static And Dynamic Finite Element Analysis*. Dover Publications, 2000.
- [28] K. St. Jacobsen and M. Dähmn. Statistics of ionospheric disturbances and their correlation with GNSS positioning errors at high latitudes. *J. Space Weather. Space Clim.*, 4:A27, 2014.
- [29] Y. Jiao and Y. T. Morton. Comparison of the effect of high-latitude and equatorial ionospheric scintillation on gps signals during the maximum of solar cycle 24. *Radio Science*, 50(9):886–903, 2015.
- [30] Y. Jiao, D. Xu, Y. Morton, and Ch. Rino. Equatorial scintillation amplitude fading characteristics across the GPS frequency bands. *Navigation*, 63(3):267–281, sep 2016.
- [31] Y. Jiao, D. Xu, Ch. L. Rino, Y. T. Morton, and Ch. S. Carrano. A multifrequency GPS signal strong equatorial ionospheric scintillation simulator: Algorithm, performance, and characterization. *IEEE Trans. Aerosp. Electron. Syst.*, 54(4):1947–1965, aug 2018.
- [32] R. E. Kalman. A new approach to linear filtering and prediction problems. *J. Basic Eng.*, 82(1):35–45, mar 1960.
- [33] R. E. Kalman and R. S. Bucy. New results in linear filtering and prediction theory. *J. Basic Eng.*, 83(1):95–108, mar 1961.
- [34] A. Koulouri, N. D. Smith, Br. C. Vani, V. Rimpilainen, I. Astin, and B. Forte. Methodology to estimate ionospheric scintillation risk maps and their contribution to position dilution of precision on the ground. *J. Geod.*, 94(2), feb 2020.
- [35] G. Li, B. Ning, Z. Ren, and L. Hu. Statistics of GPS ionospheric scintillation and irregularities over polar regions at solar minimum. *GPS Solutions*,

- 14(4):331–341, jan 2010.
- [36] X.R. Li and Y. Bar-Shalom. Performance prediction of the interacting multiple model algorithm. *IEEE Trans. Aerosp. Electron. Syst.*, 29(3):755–771, jul 1993.
- [37] D. Magill. Optimal adaptive estimation of sampled stochastic processes. *IEEE Trans. Automat. Contr.*, 10(4):434–439, oct 1965.
- [38] P. S. Maybeck. *Stochastic Models: Estimation and Control*. Academic Press, 1979.
- [39] K. P. Murphy. *Machine Learning*. MIT Press Ltd, 2012.
- [40] M. Opper. A bayesian approach to on-line learning. In *On-Line Learning in Neural Networks*, pages 363–378. Cambridge University Press, jan 1999.
- [41] A. Paul and A. DasGupta. Characteristics of the equatorial ionization anomaly in relation to the day-to-day variability of ionospheric irregularities around the postsunset period. *Radio Science*, 45(6):1–10, nov 2010.
- [42] C. Price. An analysis of the divergence problem in the kalman filter. *IEEE Trans. Automat. Contr.*, 13(6):699–702, dec 1968.
- [43] S. Priyadarshi. A review of ionospheric scintillation models. *Surveys in Geophysics*, 36(2):295–324, jan 2015.
- [44] Chuang Shi and Na Wei. Satellite navigation for digital earth. In *Manual of Digital Earth*, pages 125–160. Springer Singapore, nov 2019.
- [45] F. Sims, D. Lainiotis, and D. Magill. Recursive algorithm for the calculation of the adaptive kalman filter weighting coefficients. *IEEE Trans. Automat. Contr.*, 14(2):215–218, apr 1969.
- [46] L. Spogli, L. Alfonsi, G. De Franceschi, V. Romano, M. H. O. Aquino, and A. Dodson. Climatology of GPS ionospheric scintillations over high and mid-latitude european regions. *Ann. Geophys.*, 27(9):3429–3437, sep 2009.
- [47] Y.-Yi Sun. GNSS brings us back on the ground from ionosphere. *Geoscience Letters*, 6(1), nov 2019.
- [48] E. K. Sutton. A new method of physics-based data assimilation for the quiet and disturbed thermosphere. *Space Weather*, 16(6):736–753, jun 2018.
- [49] G. Taubin. Curve and surface smoothing without shrinkage. In *Proceedings of IEEE International Conference on Computer Vision*. IEEE Comput. Soc. Press, 1995.
- [50] B. C. Vani, M. H. Shimabukuro, and J. F. Galera Monico. Visual exploration and analysis of ionospheric scintillation monitoring data: The ISMR query tool. *Comput. & Geosci.*, 104:125–134, jul 2017.
- [51] M. Vauhkonen, P.A. Karjalainen, and J.P. Kaipio. A kalman filter approach to track fast impedance changes in electrical impedance tomography. *IEEE Trans. Biomed. Eng.*, 45(4):486–493, apr 1998.
- [52] Sr. V. Veetil, M.Aquino, H. A. Marques, and A. Moraes. Mitigation of ionospheric scintillation effects on GNSS precise point positioning (PPP) at low latitudes. *J. of Geod.*, 94(2), jan 2020.
- [53] J. Vila-Valls, P. Closas, C. Fernandez-Prades, and J. Th. Curran. On the mitigation of ionospheric scintillation in advanced GNSS receivers. *IEEE Trans. Aerosp. Electron. Syst.*, 54(4):1692–1708, aug 2018.
- [54] Br. A. Wilcox and F. Hamano. Kalman’s expanding influence in the econometrics discipline. *IFAC-PapersOnLine*, 50(1):637–644, jul 2017.
- [55] D. L. Wu. Ionospheric s4 scintillations from GNSS radio occultation (RO) at slant path. *Remote Sensing*, 12(15):2373, jul 2020.
- [56] W.-H. Yeh, Ch.-Y. Lin, J.-Y. Liu, Sh.-P. Chen, T.-Y. Hsiao, and Ch.-Y. Huang. Superposition property of the ionospheric scintillation s4 index. *IEEE Geosci. Remote. Sens. Lett.*, 17(4):597–600, apr 2020.

Appendices

6.1 Predictive distribution

In general, we denote random variables by capital letters and their realizations by lowercase letters. Here, $\{S_t\}_{t=0}^{\infty}$ and $\{Y_t\}_{t=0}^{\infty}$ are two Markov stochastic processes where the random vector $S_t \in \mathbb{R}^N$ represents the quantity of primary interest (i.e. ionospheric scintillation coefficients) and is called the state vector, and $Y_t \in \mathbb{R}^{M_t}$ is the observation vector at t . For a state space model, Markov process properties are introduced. In particular, the properties are i) $\{S_t\}_{t=0}^{\infty}$ is Markov process i.e. the conditional probability density $\pi(s_t|s_{t-1}, \dots, s_0) = \pi(s_t|s_{t-1})$, ii) $\{Y_t\}_{t=0}^{\infty}$ is Markov process with respect to the history of $\{S_t\}_{t=0}^{\infty}$ which means that $\pi(y_t|s_t, s_{t-1}, \dots, s_0) = \pi(y_t|s_t)$, and iii) process $\{S_t\}_{t=0}^{\infty}$ depends on the past observations only through its own history, i.e. $\pi(s_t|s_{t-1}, y_{t-1}, \dots, y_1) = \pi(s_t|s_{t-1})$ [20].

The predictive distribution $\pi(s_t|D_{t-1})$ (8) can be computed by the Chapman-Kolmogorov equation [39]

$$\pi(s_t|D_{t-1}) = \int \pi(s_t|s_{t-1}) \pi(s_{t-1}|D_{t-1}) ds_{t-1},$$

where $\pi(s_t|s_{t-1})$ is the transition probability and depends on the evolution model (3), and $\pi(s_{t-1}|D_{t-1})$ is the posterior density of the previous time step. Under Gaussian condition for the noise and the prior, the posterior is Gaussian i.e. $\pi(s_{t-1}|D_{t-1}) \sim \mathcal{N}(\hat{s}_{t-1}, \Gamma_{s_{t-1}|D_{t-1}})$, where \hat{s}_{t-1} is the mean and $\Gamma_{s_{t-1}|D_{t-1}}$ is the posterior covariance at time $t-1$.

$$\pi(s_t|D_{t-1}) \propto \int \exp\left(-\frac{1}{2}(s_t - s_{t-1})^T \Gamma_{n_t}^{-1}(s_t - s_{t-1})\right) \exp\left(-\frac{1}{2}(s_{t-1} - \hat{s}_{t-1})^T \Gamma_{s_{t-1}|D_{t-1}}^{-1}(s_{t-1} - \hat{s}_{t-1})\right) ds_{t-1}.$$

6.2 Coefficient of the observation matrix

To estimate the coefficients of matrix A_t , we first find the element where the IPP $x_j(t) = (x_j^{lat}, x_j^{lon})$ of observation $y_t(x_j)$ is projected to. If point $x_j(t)$ lies on element \mathcal{T}_k with nodes x_{p_k} ($k = 1, 2, 3$)¹, then the observation $y_t(x_j)$ is expressed as a linear combination of the three basis functions which have support on this triangular element denoted by $\phi_{p_k}(x) = a_{p_k} x^{lat} + b_{p_k} x^{lon} + c_{p_k}$. Then, $y_t(x_j) = \sum_{k=1}^3 \phi_{p_k}(x_j(t)) s_{p_k}$, where s_{p_k} are the scintillation values at the corresponding element's nodes x_{p_k} . Now, the coefficients $\{a_{p_k}, b_{p_k}, c_{p_k}\}$ of the basis functions can be estimated by solving a set of linear equations where $\phi_{p_k}(x_{p_l}) = 1$ when $l = k$ and $\phi_{p_k}(x_{p_l}) = 0$ when $l \neq k$. Then we estimate $\phi_{p_k}(x_j(t)) = a_{jk}$. Hence S_4 value $y_t(x_j)$ is a weighted sum of the S_4 values of the nodes of the element where x_j is located. An alternative way to estimate these coefficients is to use the isoparametric mapping [27].

¹This is a local indexing to distinguish the three nodes of element \mathcal{T}_k